



Stochastic analysis of imperfection sensitive composite cylinders using realistic imperfection models

Jendi Kepple^{*a, b}

PhD Research Candidate

Manudha Herath^a, Garth Pearce^a, Gangadhara Prusty^a, Rodney Thomson^{b, c}

^a School of Mechanical and Manufacturing Engineering, The University of New South Wales, Kensington, NSW 2032, Australia.

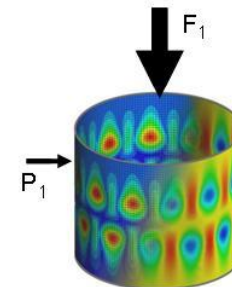
^b Cooperative Research Centre for Advanced Composite Structures, 1/320 Lorimer Street, Port Melbourne, Victoria 3207, Australia.

^c Advanced Composite Structures Australia Pty Ltd, 1/320 Lorimer Street, Port Melbourne, Victoria 3207, Australia.

*Corresponding author: jendi.kepple@unsw.edu.au, +61 421 074 881



UNSW
THE UNIVERSITY OF NEW SOUTH WALES





Introduction

- DESICOS Project: New Robust Design Guideline for Launch Vehicle Structures
- Strong requirement for more robust, lighter and cheaper launch vehicle structures
- Unstiffened cylindrical shells used in launch vehicles [1,2]
- Shells are prone to buckling and are highly sensitive to imperfections which arise during the manufacturing process [3–5]
- Imperfections facilitate drastic variation of buckling load from theoretically perfect structure [6,7].

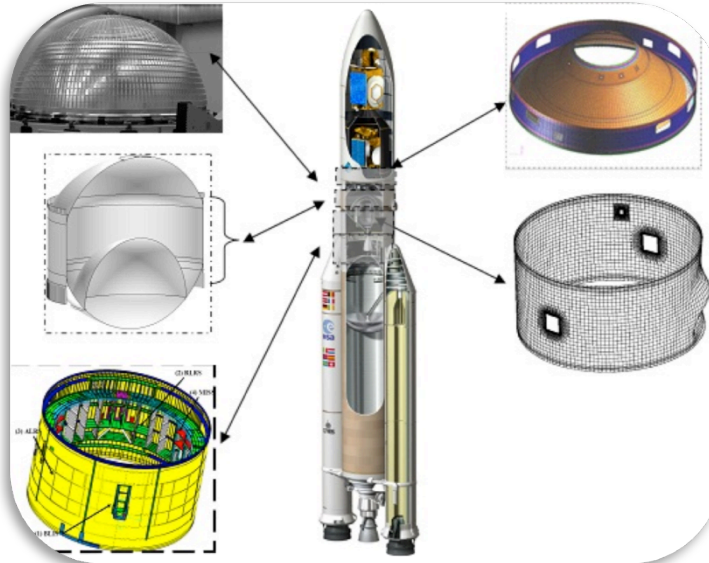


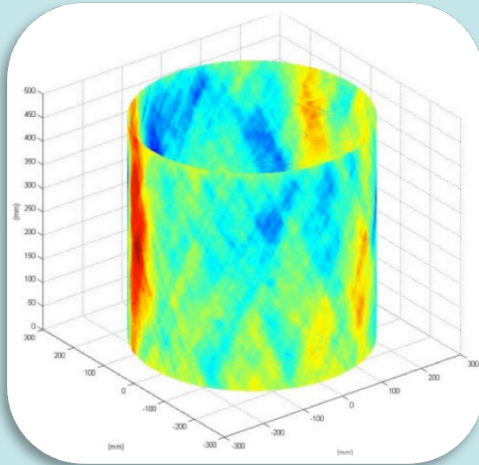
Figure 1. Ariane 5 launch vehicle. [1]



Imperfection Types

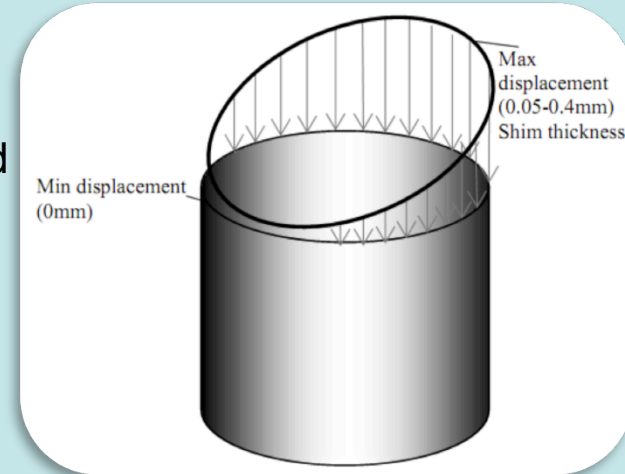
Geometric

global and/or localised variations of the radial distance of points on the surface of the cylinder to the geometric centre



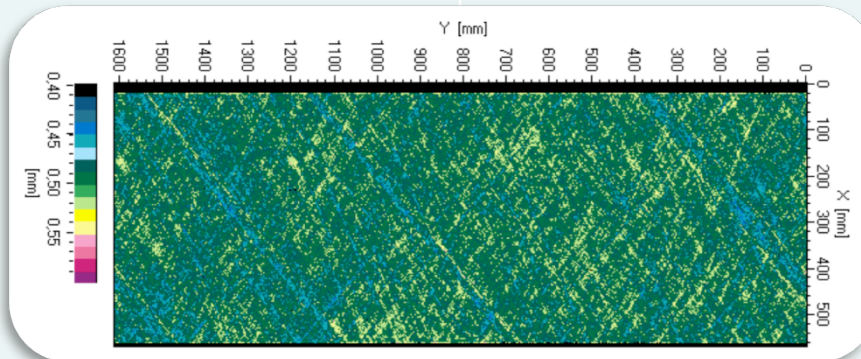
Loading

unevenness or uncertainty of the applied load



Thickness

arise from ply gaps, overlaps and changes in the resin distribution



Material

variations in the Young's moduli, Poisson's ratios and shear moduli



Current Design Guideline

- The current design guidelines [8] for imperfection sensitive shells are based on the NASA-SP 8007 [9] which dates from 1968.

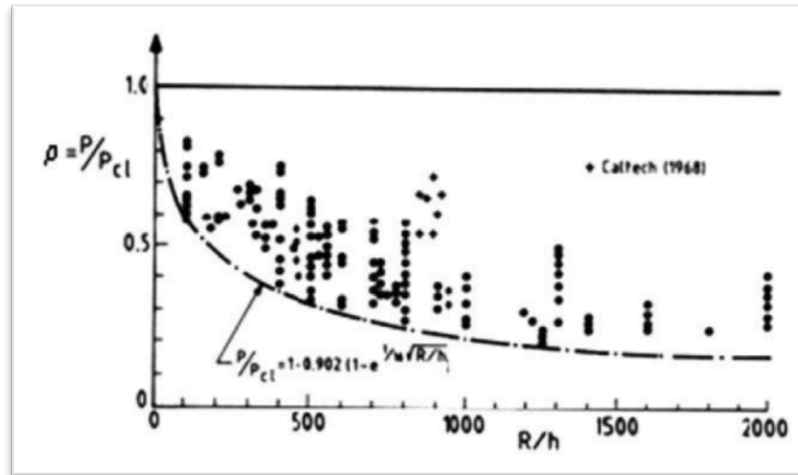


Figure 2. Knock-down factors are derived from empirical data in NASA SP-8007. [9]

- First calculate the theoretical buckling load of a geometrically perfect structure by performing a linear bifurcation analysis using closed-form equations.
- Theoretical buckling load is then reduced by applying an empirical knockdown factor to account for the differences between theory and test.
- From recent literature [10,11], the NASA-SP 8007 knockdown factors were determined to be exceedingly conservative.
- Unsuitable for shells constructed from modern manufacturing processes and materials such as composites.



Analytical and Numerical Methods

- In 1945, Koiter [3] pioneered an analytical method to incorporate ‘classical’ *geometric imperfections*.
- Effort to determine the effects of *initial geometric imperfections* on the buckling response by analytical means through digital computers [12,13].
- Realistic imperfections diverge from the strictly sinusoidal imperfection shapes [7,14–16].
- Also possess a variety of ‘unclassical’ imperfection types.
- ‘Unclassical’ imperfections include:
 - *thickness imperfections*,
 - *material property imperfections* and,
 - *initial loading imperfections* [17].
- Computational power available today and structural analysis codes enables stochastic analysis [17–22].
- Stochastic methods facilitate useful robust simulation studies.
- Sheer number of possible imperfections means it is impossible to develop design criteria using experimental data alone.
- Numerical investigation can be achieved more rapidly and robustly than experimental investigation.
- Imperfections imposed on numerical models are representative of real imperfections.
- Realistic modelling is also important to prevent excessively conservative designs and to ensure an optimised, cost-efficient and light-weight structure.



Stochastic Methods

- Stochastic simulation of geometric imperfections has been achieved previously.
- **Method of separation** [23] and **spectral representation method** [21,24,25] have previously been used to generate geometric imperfections on both isotropic [23] and orthotropic [18,19] cylinders.
- Geometric imperfections treated as random fields.
- In [18,19], evolutionary power spectra of the geometric imperfections were used in the spectral representation method to generate one hundred cylinders with geometric imperfections that conform to the statistical margins of the original experimentally tested shells.
- **Previous work does not account directly for thickness and material imperfections.**
- Experimentally measured thickness imperfections added to analysis and material imperfections were inferred using a **finite-element based moving-window averaging technique**.
- To extend the work of [19], this paper analyses existing thickness data from nominally identical composite cylinders to ascertain the characteristics of the thickness imperfections.
- This method characterises thickness imperfections and also takes into account ply gaps and resin distribution independently.
- Imperfection characteristics used to generate stochastic results for thickness imperfections from which material imperfections can be inferred.
- Virtual cylinders can be rapidly numerically studied to determine the role that thickness and material imperfections play on the buckling behaviour, without the prohibitively large expense of fabricating and testing of a large number of cylinders.



Experimental Background

- Imperfection database of eight nominally identical CFRP IM7/8552 UD ultrasonic scanned and tested cylinders (labelled non-consecutively from Z15-Z26) acquired from a joint DLR-ESA research program [7,26].
- The DLR-ESA cylinders representative of imperfection sensitive design.
- Sensitivity of the axial buckling load to each imperfection type is magnified.

Table 1. Nominal properties of DLR-ESA cylinders [7].

Property	Nominal Data
Total length (mm)	540
Free length (mm)	500
Radius (mm)	250
Lay up	[±24/±41]
Ply Thickness (mm)	0.125
Longitudinal Young's modulus, $E_{1,c}$ (GPa)	157.4
Transverse Young's modulus, $E_{2,c}$ (GPa)	10.1
Shear modulus, $G_{12,c}$ (GPa)	5.3
Shear modulus, $G_{23,c}$ (GPa)	4.0

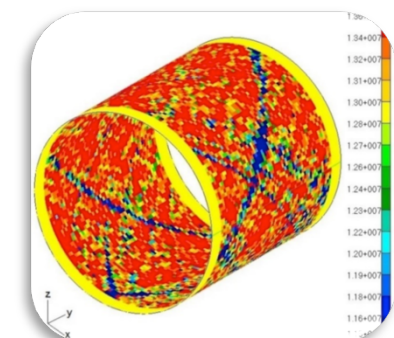
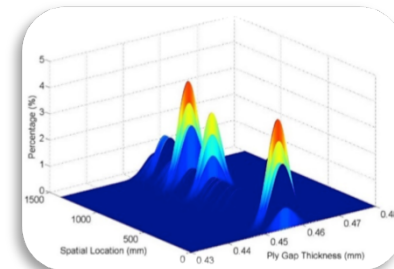
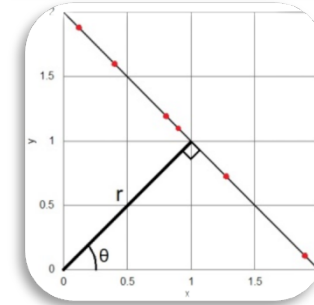
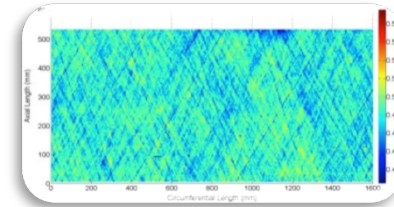
- Thickness imperfection readings provided as a set of pixels.
- Each pixel represents one thickness measurement.
- Thickness measurements are discrete, each cylinder was represented by 513 pixels in the circumferential direction and 183 pixels in the axial direction = total number of 93,769 pixels.



Method

1. Hough Transform [27] used to separate ply gaps and overlaps from variations in matrix.
2. Matrix properties characterised by power spectrum estimates.

$$E \left[|f(x)|^2 \right] = 2 \int_0^{\infty} S(\omega, x) d\omega$$
3. Power spectrum $S(\omega)$ is homogenous if depends only on frequency. Evolutionary $S(\omega, x)$ if depends on frequency ω and spatial localization (x). Improved methods of estimating the power spectrum include:
 1. Short Time Fourier Transform (STFT) [28],
 2. Harmonic Wavelet Transform [29] and,
 3. Method of Separation.
4. Monte Carlo analysis used to generate new ply gap imperfections.
5. Spectral representation method used to generate new resin-matrix distribution imperfections.
6. Monte-carlo results superimposed onto spectral representation results.
7. Material imperfections inferred from thickness imperfections through moving-window averaging technique [19].
8. New material imperfections assembled into finite element analysis and compared with experimental results.





The Hough Transform

- Imperfection database of eight nominally identical CFRP IM7/8552 UD ultrasonic scanned and tested cylinders (labelled non-consecutively from Z15-Z26) was acquired from a joint DLR-ESA research program. [7,26]
- Available as a collection of pixels, each pixel = one thickness measurement.
- Example of ultrasonic measured thickness imperfections of the Z23 shell structure shown in Figure 3.
- Deepest imperfections form lines in the exact angles of the composite lay-up.
- Hough transform used to determine collinear points.

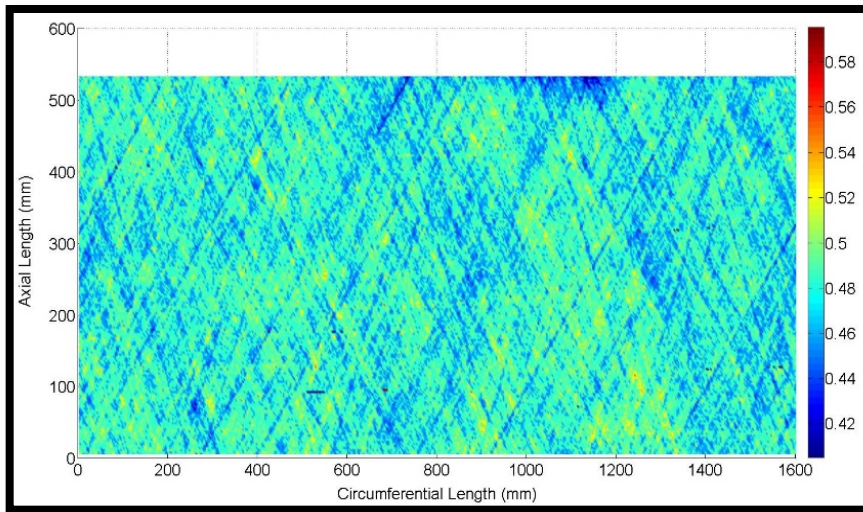


Figure 3. Ultrasonic-scanned real thickness imperfections on the Z23 cylinder. [7]

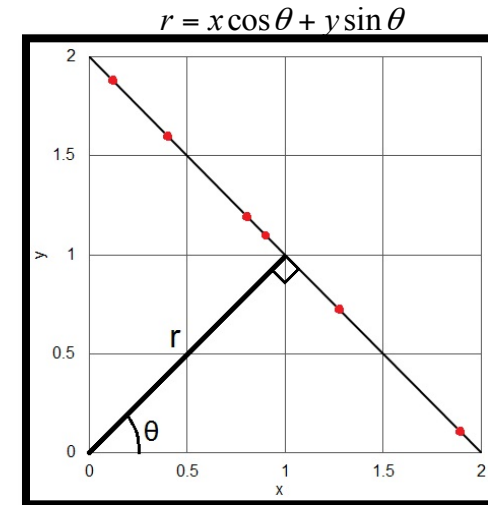


Figure 4. The Hough transform discovers points that are collinear.



The Hough Transform Continued

- Scan data is periodic in the circumferential direction because it is captured from a cylinder.
- Ply gaps and overlaps therefore enter and leave the domain at the circumferential extremities and reappear at the opposite end.
- Data from the left of the domain was copied over to the right and vice versa as shown in Figure 5.
- Once the points are collected, the duplicated regions are deleted.

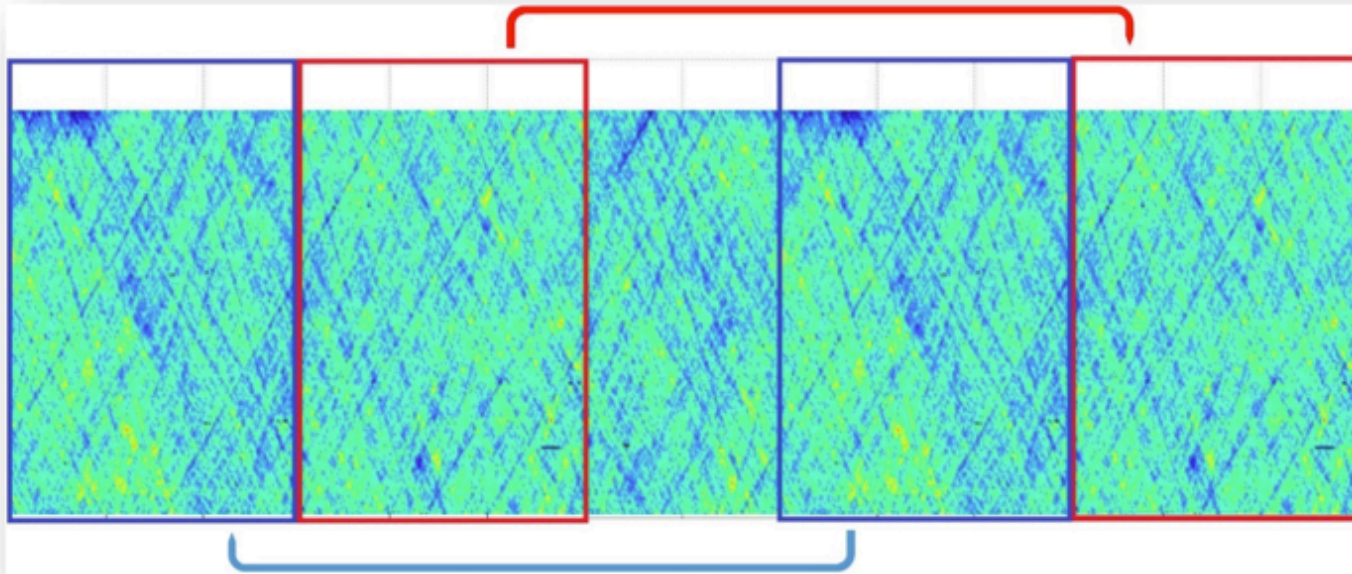


Figure 5. Simulated period boundary conditions by way of duplicated data at either end of the domain.



The Hough Transform Results

- Figures 6(a) and 7(a) show the thickness imperfections of the Z26 and Z17 cylinders [7].

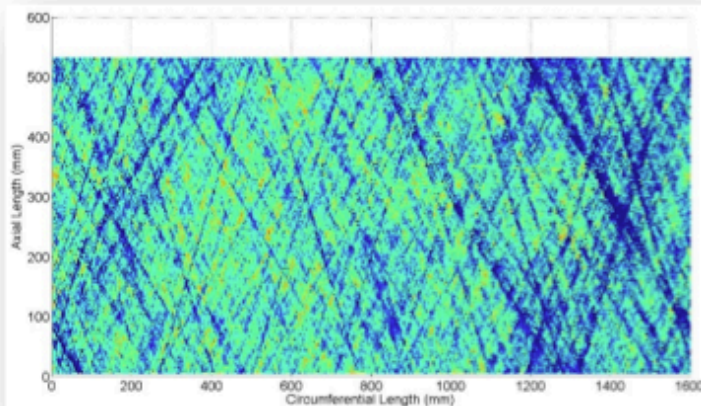


Figure 6(a). Z26 Cylinder.

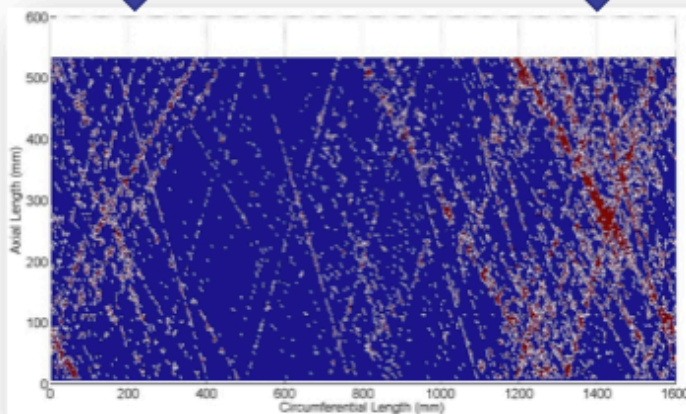


Figure 6(b). Points removed from Z26 cylinder are shown in red.

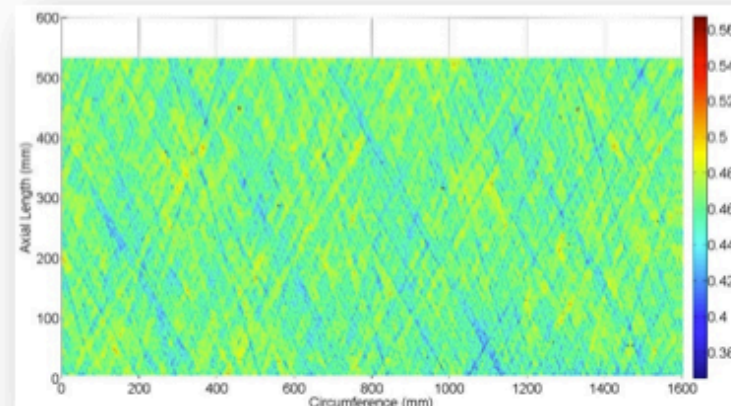


Figure 7(a). Z17 Cylinder.

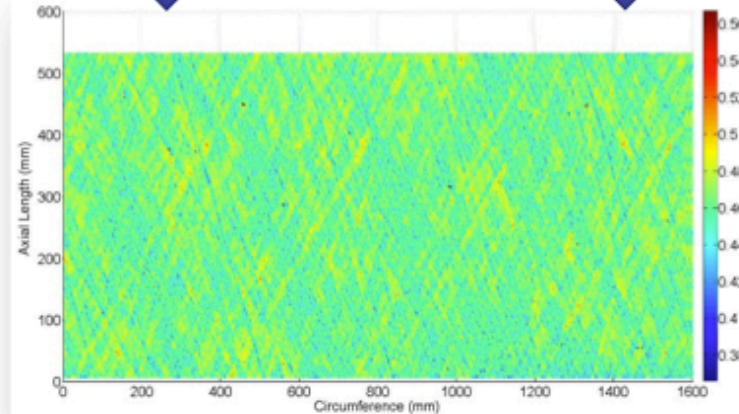


Figure 7(b). Lines removed from Z17 cylinder reveal the distribution of the matrix imperfections.



Power Spectrum Estimation Techniques

- A 1D benchmark spectra known as the Kanai-Tajimi spectrum [30] was used to validate the MATLAB script for obtaining the power spectrum of the thickness imperfections.
- The Kanai-Tajimi spectrum is defined by the separable frequency $S(\omega)$ and spectral $g(x)$ components shown below [21]:

$$S(\omega) = \frac{1 + 4\zeta^2 \left(\frac{\omega}{\omega_0} \right)^2}{\left[\left(1 - \left(\frac{\omega}{\omega_0} \right)^2 \right)^2 + \left(2\zeta \frac{\omega}{\omega_0} \right)^2 \right]}$$

$$g(x) = \frac{e^{-0.25x} - e^{-0.5x}}{0.25}$$

- Where the parameters $\omega_0 = 10$ rad/mm and $\zeta = 0.24$ represent the natural frequency and damping ratio, respectively. The exact spectrum is shown below.

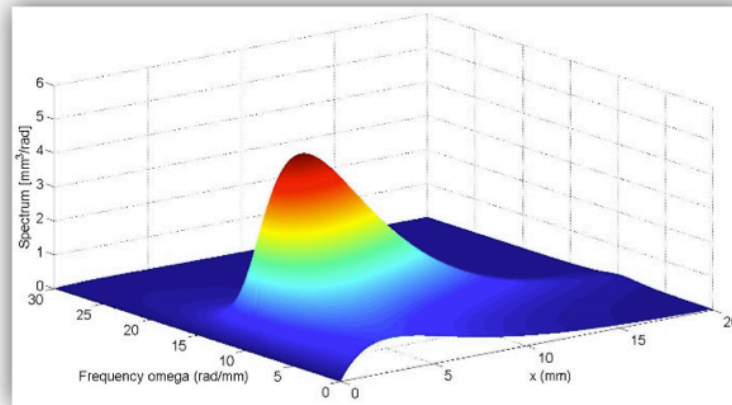


Figure 8. Kanai-Tajimi Spectrum



Exact Spectrum

$$S(\omega) = \frac{1 + 4\zeta^2 \left(\frac{\omega}{\omega_0}\right)^2}{\left[1 - \left(\frac{\omega}{\omega_0}\right)^2\right]^2 + \left(2\zeta \frac{\omega}{\omega_0}\right)^2} \quad g(x) = \frac{e^{-0.25x} - e^{-0.5x}}{0.25}$$

- 1D separable spectrum
- Damping ratio: $\zeta = 0.24$
- Natural frequency: $\omega_0 = 10\text{rad/mm}$

Homogenous spectrum

$$\mathcal{S}_h(\omega) = E \left[\frac{1}{2\pi L} \cdot \left| \int_0^L f^{(i)}(x) \cdot e^{-i\omega x} dx \right|^2 \right]$$

- L is the total sample length
- estimates the frequency distribution of a spectrum
- no consideration towards spatial variation or modulating envelope

Method of separation

$$S(\omega, x) = S_h(\omega) \cdot g(x)$$

$$\mathcal{S}_h(\omega) = E \left[\frac{1}{2\pi L} \cdot \left| \int_0^L f^{(i)}(x) \cdot e^{-i\omega x} dx \right|^2 \right] \quad g(x) = \frac{E \left[\left| f^{(i)}(x) \right|^2 \right]}{2 \int_0^\infty \mathcal{S}_h(\omega) d\omega}$$

- Focuses on energy variations in both the frequency and spatial axes
- Input samples $f^{(i)}(x)$ need to be approximately separable so frequency and spatial components can be dealt with separately
- Narrow-banded spectra: limited to a specified frequency range, to avoid large distribution errors
- spatial axis must be approximately uniformly modulated and must not vary significantly

STFT with rectangular windowing function

$$\mathcal{S}_j(\omega, x) = E \left[\frac{1}{2\pi T} \cdot \left| \int_{\chi-T/2}^{\chi+T/2} f^{(i)}(x) w(x - \chi^j) \cdot e^{-i\omega x} dx \right|^2 \right]$$

$$w(x) = \begin{cases} 1 & -T/2 \leq x \leq T/2 \\ 0 & \text{elsewhere} \end{cases}$$

- Emphasizes spectrum at specific spatial locations ($x = \chi$) also known as windows
- Suppresses spectrum components located further away
- Unable to achieve simultaneous localization in both frequency and space [28]
- Width of the window reduced to achieve greater accuracy in the spatial axes, the STFT will sacrifice information in the frequency axes and vice versa.



Power Spectrum Estimation Techniques

Exact Spectrum

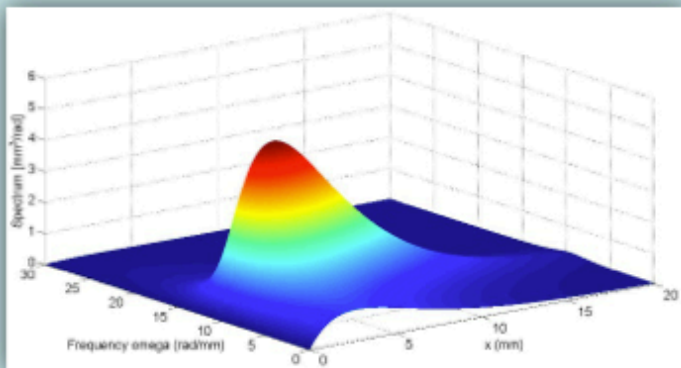


Figure 9. Kanai-Tajimi Spectrum

Homogenous spectrum

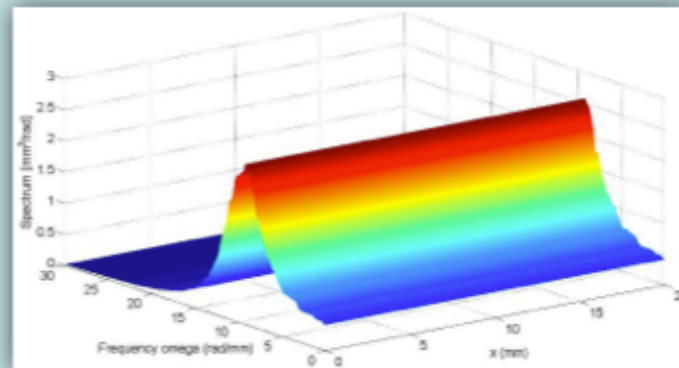


Figure 10. Homogenous spectrum estimation

Method of separation

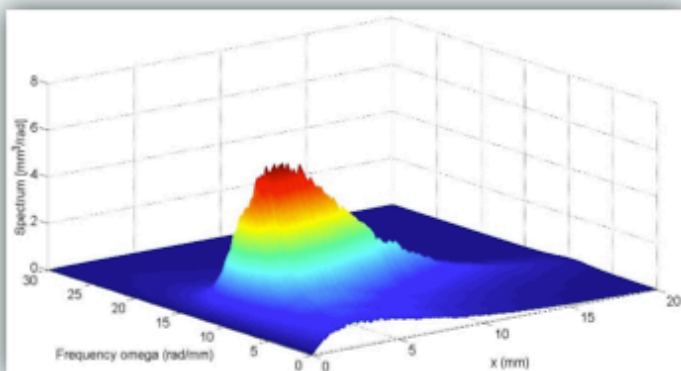


Figure 11. Method of Separation spectrum estimation

STFT with rectangular windowing function

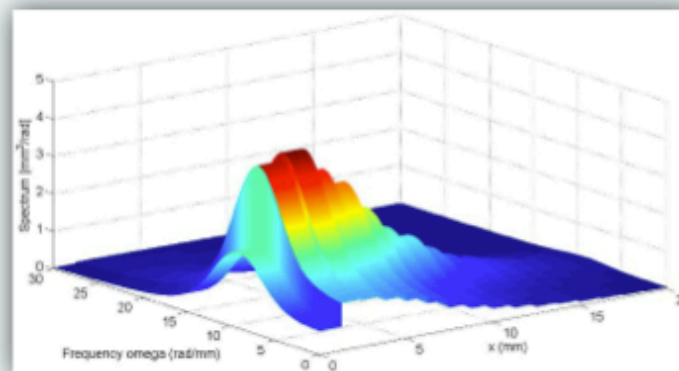
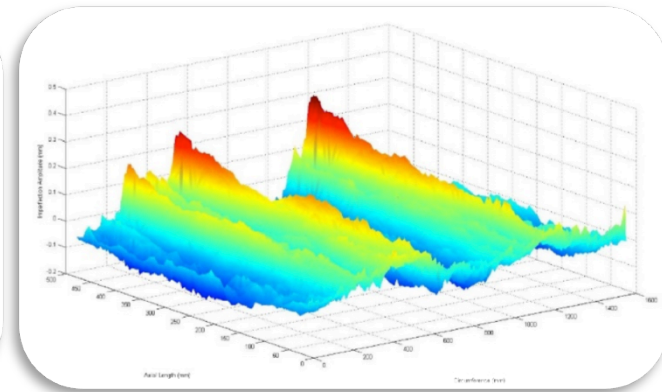
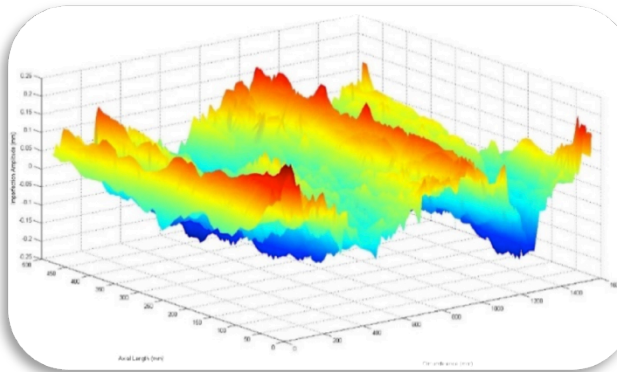
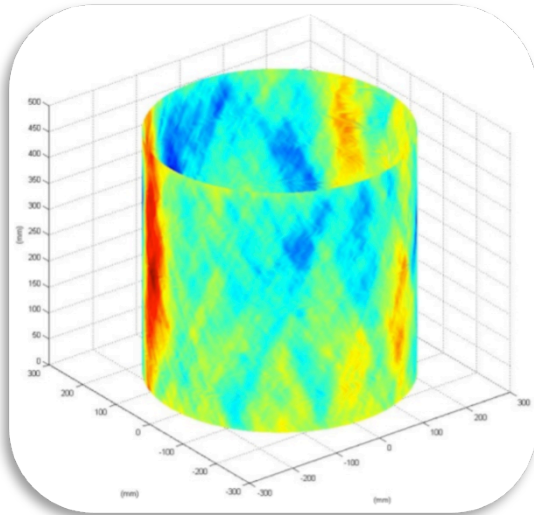


Figure 12. STFT spectrum estimation



Method of Separation

- Method of separation provides the most accurate spectrum estimate of the Kanai-Tajimi spectrum for the least number of stochastic inputs.
- Method of separation has also been used to estimate the evolutionary power spectrum of geometric imperfections in shells. [18,19,23]



Figures 13,14 and 15. Geometric imperfections have been successfully replicated using the method of separation.

- Due to these advantages and provided that the distribution of the matrix met separability criteria, the method of separation was first used in an attempt to estimate the power spectrum of the matrix imperfections.



Spectral Analysis of Matrix Imperfections: 1D STFT



- Used to estimate the extent of the narrow-bandedness of the power spectrum of the thickness imperfections in order to ensure reduced errors in utilising the 2D method of separation.
- estimate obtained at six equally spaced positions by a non-overlapping rectangular window of length $L/6$ (where L is the circumference of the cylinder)
- Circumferential direction of the lowest axial reading (without the removal of any ply gaps) of the Z15-Z26 cylinders [7] is shown in Figure 16(a), frequency-side view shown in Figure 16(b). Other spectrum based estimates for circumferential imperfection readings at various axial lengths exhibit similar behaviour.

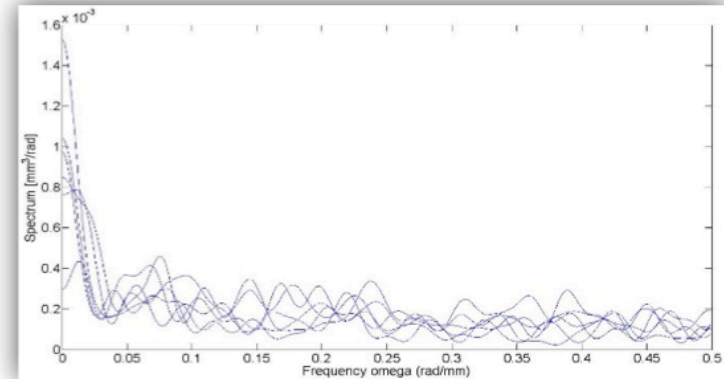
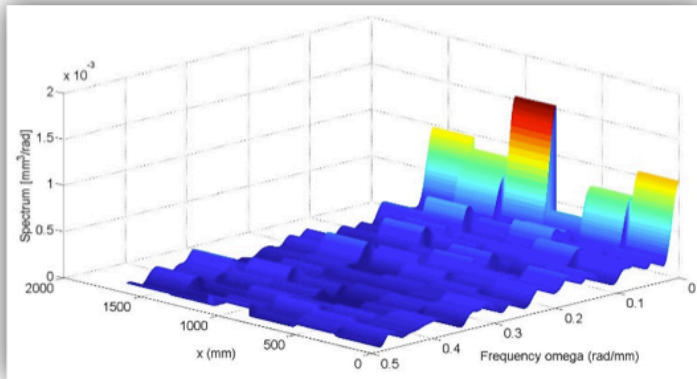


Figure 16(a). STFT spectrum estimates. Figure 16(b). Side view, amplitude in the frequency spectrum.

- Approximately 40% of the variation of the energy distribution in the frequency component is limited to small fixed bandwidth (between 0-0.05rad/mm).
- Large section of the energy distribution is represented by the remaining frequencies.
- Not sufficient to warrant the use of the method of separation which requires approximately 90% or more of the main lobe of the energy distribution to be located within a small band-width to avoid large distribution errors [21].



Spectral Analysis of Matrix Imperfections: 1D STFT



- Ply-gap imperfections were removed, only minor improvements in the narrow-bandedness of the STFT spectrum estimate for variations in the matrix.
- Distributions in the matrix imperfections are largely random and contain very few patterns.
- Variations in the spatial direction are not uniformly modulated and diverge strongly.
- Method of separation is unsuitable for this imperfection type.
- The assumption of separability may be worked-around by partitioning the space-frequency spectrum into parts that are of themselves narrow-banded or approximately separable [25].
- However, the spectrum estimates shown in Figures 14(a) and (b) indicate that the spectrum would have to be partitioned into a very large number of smaller sections.
- Each section must then be analysed by the method of separation and then stitched back together to form the complete spectrum.
- The time required to construct the final spectrum may outweigh any inaccuracies produced by the 2D STFT method.



Spectral Analysis of Matrix Imperfections: 2D STFT



- The 2D STFT can be derived from the generalised homogenous periodogram [23]:

$$S_{ii}^0(\omega) = E \left[\frac{1}{(2\pi)^2 L_1 \cdot L_2 \dots L_n} \cdot \left| \int_0^{L_1} \dots \int_0^{L_n} f^{(i)}(x) \cdot e^{-i(\omega_n x_n)} dx_n \dots e^{-i(\omega_1 x_1)} dx_1 \right|^2 \right]$$

- The 2D STFT is therefore:

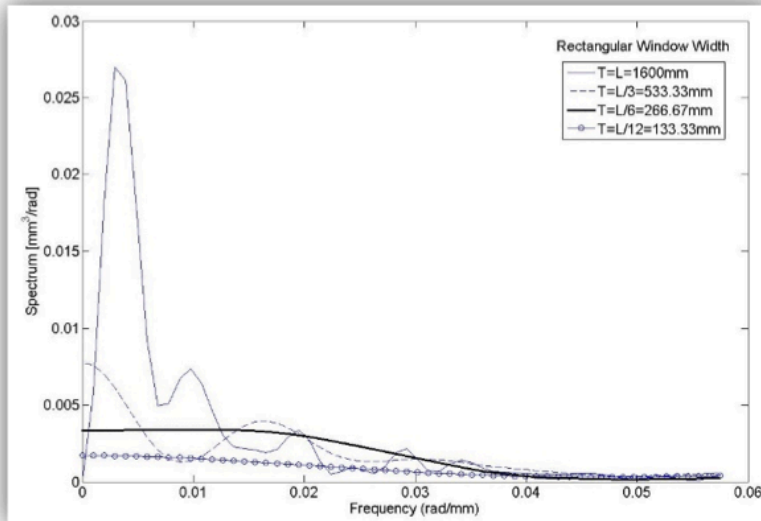
$$S_j^0(\omega_1, \omega_2, x, y) = E \left[\frac{1}{4\pi^2 T_x T_y} \cdot \left| \int_{\chi - \frac{T_x}{2}}^{\chi + \frac{T_x}{2}} \int_{\Upsilon - \frac{T_y}{2}}^{\Upsilon + \frac{T_y}{2}} f^{(i)}(x, y) w(x - \chi^j, y - \Upsilon^j) \cdot e^{-i(\omega_1 x + \omega_2 y)} dx dy \right|^2 \right]$$

- Where x and y correspond to the circumferential and axial directions respectively and T_x and T_y are the widths of the rectangular windowing functions in the circumferential and axial direction. χ^j and Υ^j correspond to the centre spatial location of the windows to be examined in the circumferential and axial directions.

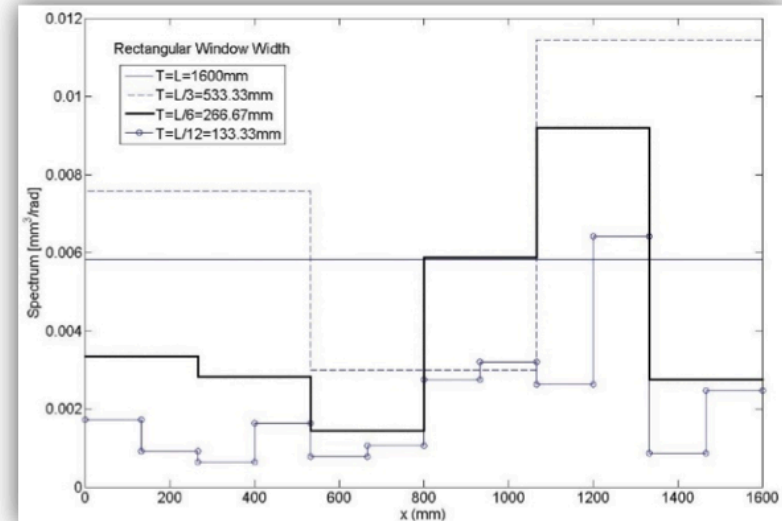


Spectral Analysis of Matrix Imperfections: 2D STFT

- 2D STFT coded into MATLAB
- Imperfections due only to changes in the resin distribution of the Z15-Z26 cylinders added as input functions.
- Resulting 4D function is difficult to plot so data in the frequency and spatial axes in the axial direction have been suppressed for ease of viewing Figures 17(a) and (b).



(a)



(b)

Figure 17. Comparison of various rectangular window widths for 2D STFT in the circumferential direction only (axial values suppressed for ease of viewing), (a) reduction in accuracy of frequency estimate with decreasing window size and (b) increase in accuracy of spatial estimate with decreasing window size.



Spectral Representation of Matrix Imperfections

- The spectral representation for a 2D Gaussian random field is as follows [23]:

$$f^{(i)}(x, y) = \sqrt{2} \sum_{n=0}^{N_1-1} \sum_{m=0}^{N_2-1} \left[A_{nm} \cos(\omega_{1n}x + \omega_{2m}y + \phi_1^{(i)}) + A_{nm} \cos(\omega_{1n}x - \omega_{2m}y + \phi_2^{(i)}) \right]$$

- Where

$$A_{nm} = \sqrt{2 \cdot S(\omega_{1n}, \omega_{2m}, x, y) \cdot \Delta\omega_1 \cdot \Delta\omega_2}$$

- Where N_1 and N_2 determine the discretization within the active frequency range of the circumferential and axial axes and $\phi_1^{(i)}$ and $\phi_2^{(i)}$ are the (i)th realizations of N_1 and N_2 independent phase angles that are uniformly distributed in the range $[0, 2\pi]$.
- A MATLAB code produced 100 new realisations of the random field. Examples are below and are compared to actual imperfections.

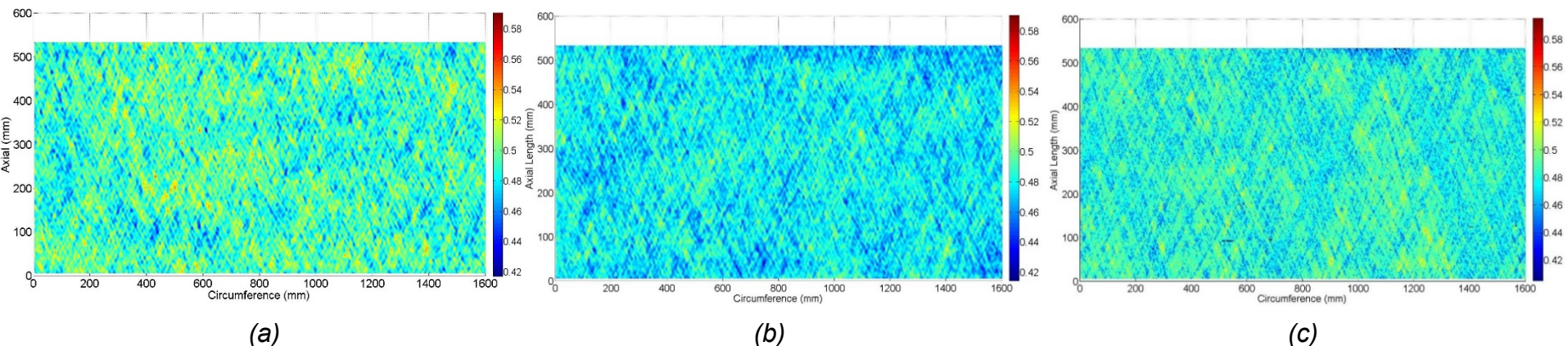
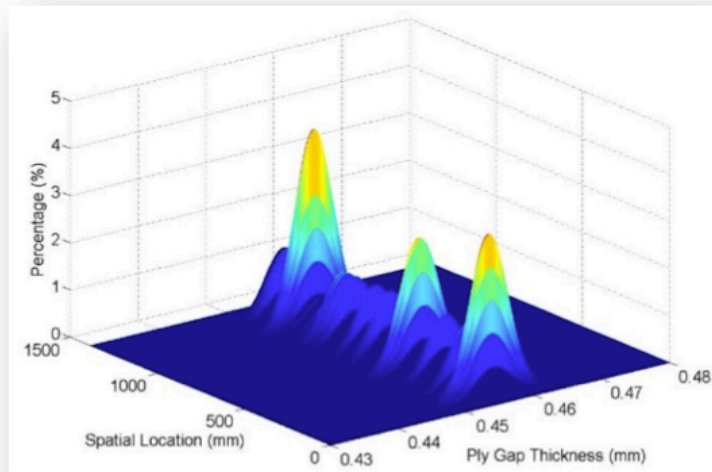


Figure 18 (a) and (b). Sample matrix imperfections generated from the spectral representation method. (c) Actual matrix imperfections from the Z23 cylinder with the most prominent gap and overlap lines removed.

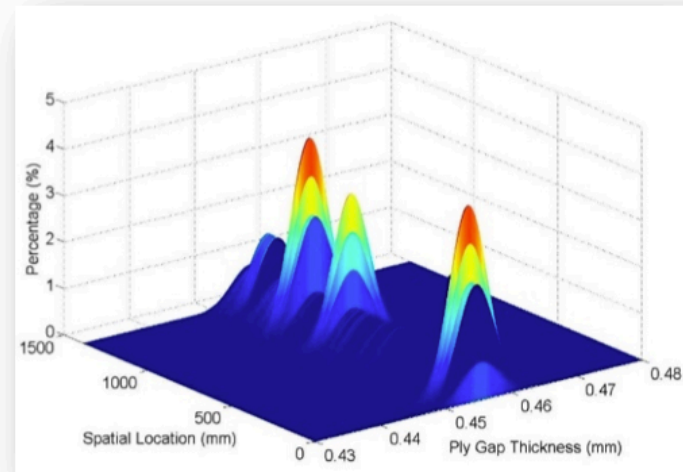


Monte-Carlo Analysis of Ply Gaps and Overlaps

- Further analysis on isolated ply gaps and overlaps of eight CFRP IM7/8552 UD real cylinders [7] provide the statistical properties to generate new imperfections for stochastic analyses.
- The properties of most interest are: the variation in the thickness of the lines, the number of lines at various angles and the spatial location of these lines.
- The thickness amplitudes of the lines were collected and assumed to be normally distributed.
- Similarly, the spatial distribution of these lines were recorded and utilised to construct a unique probability distribution as shown in Figure 19(a) and (b) for the -24 degree and 24 lines respectively.



(a)



(b)

Figure 19. (a) Probability distribution of -24 degree gap lines and (b) 24 degree gap lines.



Stochastic Samples

- A Monte-Carlo random number generator generated 100 new stochastic fields.
- Include variations in that are representative of the statistical properties of the ply gaps in the original eight nominally identical shells:
 - *variation in thickness of the lines,*
 - *spatial distribution and location of these lines and;*
 - *quantity of ply gaps/overlaps.*
- The results from this procedure were superimposed onto the stochastically generated matrix imperfections. Examples of the results of this process are shown below:

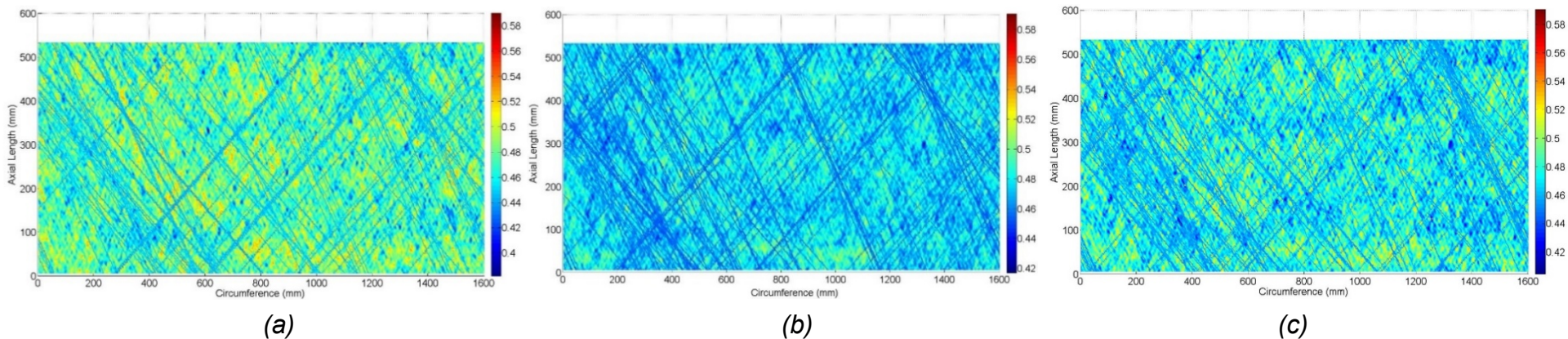


Figure 20 (a-c). Samples of thickness imperfections generated from spectral representation and Monte-Carlo methods.



Moving-Window Averaging Technique

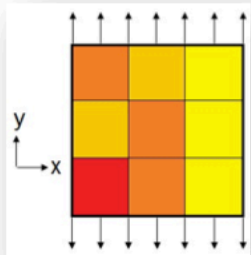
- The scan data from the thickness readings was captured at a higher resolution than the benchmark mesh density; each element contained approximately 9 pixels.
- The corresponding material properties per pixel were averaged over the entire element to produce the same strains and curvatures as an analysis with nine times the number of elements.
- A version of the moving window averaging technique introduced in [32] and modified by [19] was used to achieve the average properties.
- The modified moving window averaging technique provides the composite-characterising extensional, bending and coupling matrix for each element by solving the following equation:

$$\begin{bmatrix} N_x \\ N_y \\ N_{xy} \\ M_x \\ M_y \\ M_{xy} \end{bmatrix} = \begin{bmatrix} A_{11} & A_{12} & A_{13} & B_{11} & B_{12} & B_{13} \\ A_{21} & A_{22} & A_{23} & B_{21} & B_{22} & B_{23} \\ A_{31} & A_{32} & A_{33} & B_{31} & B_{32} & B_{33} \\ B_{11} & B_{12} & B_{13} & D_{11} & D_{12} & D_{13} \\ B_{21} & B_{22} & B_{23} & D_{21} & D_{22} & D_{23} \\ B_{31} & B_{32} & B_{33} & D_{31} & D_{32} & D_{33} \end{bmatrix} \begin{bmatrix} \epsilon_x^0 \\ \epsilon_y^0 \\ \gamma_{xy}^0 \\ \kappa_x \\ \kappa_y \\ \kappa_{xy} \end{bmatrix}$$

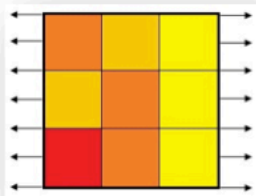


Moving-Window Averaging Technique

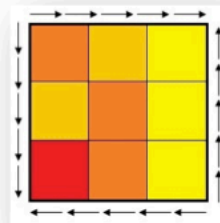
- For each element in the full analysis of the cylinder, separate finite-element analyses were performed on squares which contained the material properties of the corresponding nine pixels.
- A variety of unitized axial, shear and bending loads satisfying the left hand side the ABD matrix equation were individually implemented on the squares as described in Figure 21.
- The strains and curvatures from the analyses were recorded.
- The ABD matrix equation was inverted using MATLAB and the A, B, and D matrices were solved for each element.



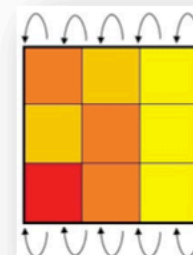
(a)



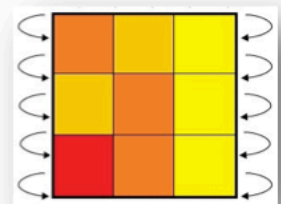
(b)



(c)



(d)



(e)

Figure 21. Distributed unitized loads applied to FE squares of 9 elements in the (a) uni-axial y direction, (b) uni-axial x direction, (c) shear on edges, (d) moment about x -axis and (e) moment about y -axis.



Moving-Window Averaging Technique



- The evolution of the A, B and D matrices for a random stochastically generated cylinder is shown in Figures 22-24.
- The technique successfully captures localized changes in material properties from variations in the matrix, ply gaps and overlaps.

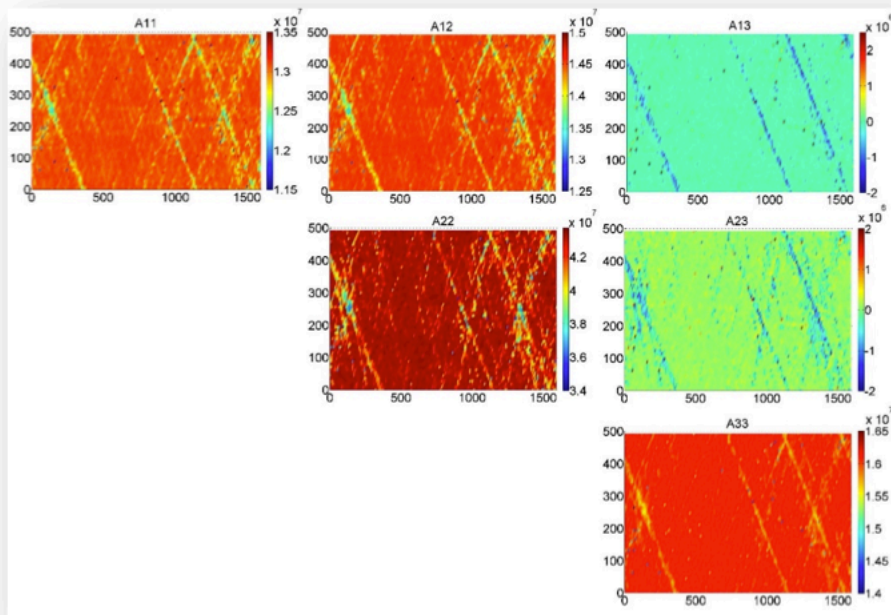


Figure 22. Evolution of the extensional matrix on a stochastically generated cylinder. Units in N/m.

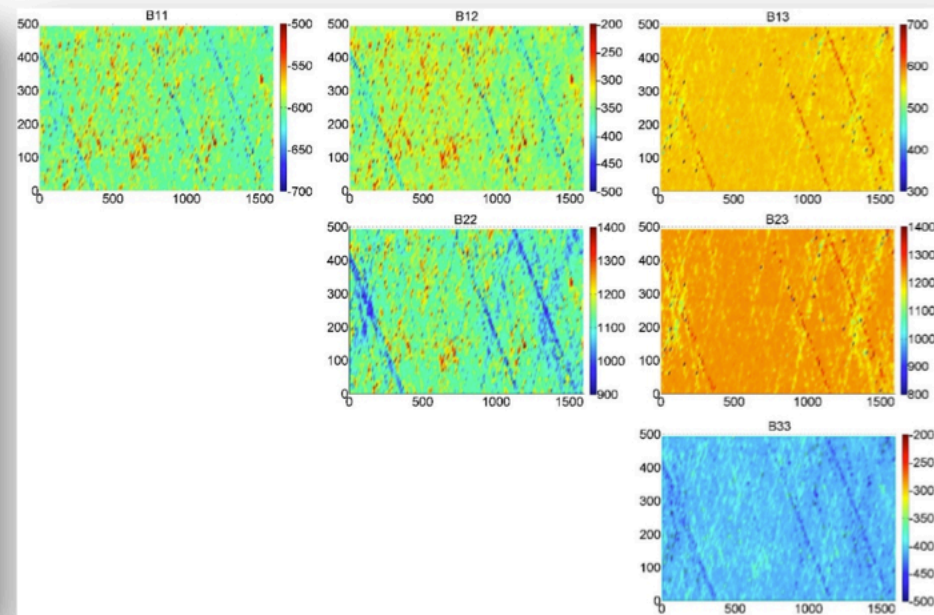


Figure 23. Evolution of the coupling matrix on a stochastically generated cylinder. Units in N.



D Matrix

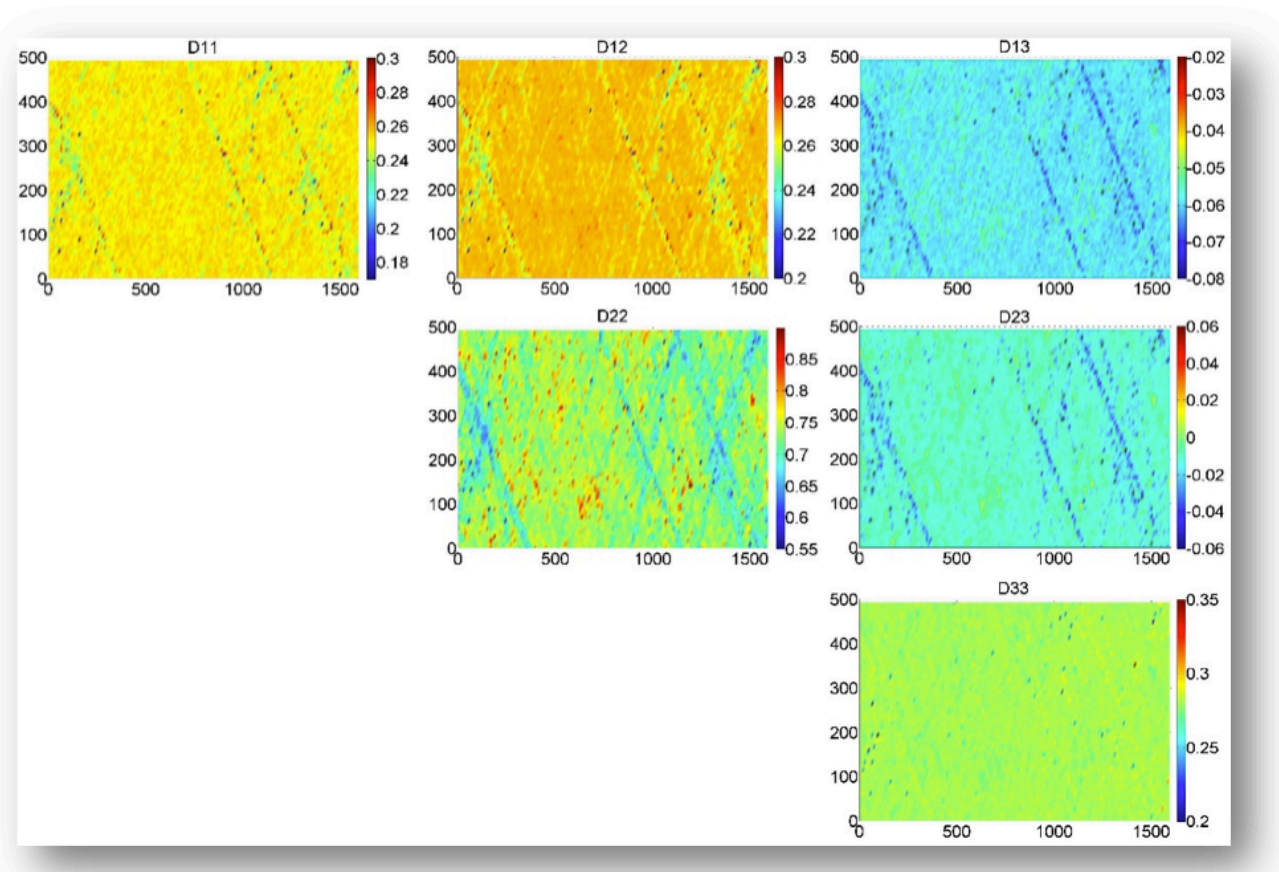


Figure 24. Evolution of the bending matrix on a stochastically generated cylinder. Units in Nm.



Numerical Results

- The cylinders were analysed under compressive load using ANSYS APDL.
- Clamped boundary conditions were applied.
- Displacement controlled shortening was induced to the top of the cylinder which increased following a linear ramp law.
- Linear 4-node layered shell elements used.
- Refinement study was conducted on a perfect cylinder to determine optimum mesh density. Between 1,500 and 80,000 elements were analysed. Benchmarked model contains 171 elements in the circumferential direction and 67 elements in the axial direction.
- A non-linear implicit slow dynamic solver was used with full Newton-Raphson iteration.
- Two non-linear static solvers were initially trialled, one used artificial damping and the other trialled the arc-length method, however convergence was very difficult to achieve during the buckling event.
- The buckling load of the perfect cylinder was determined to be 38.2kN.
- Displacement behaviour morphs from three axial half-waves during buckling to a stable post-buckling pattern at 1mm shortening with two axial half-waves. This behaviour coincides with the post-buckling patterns shown in [7,18,19].



Numerical Results

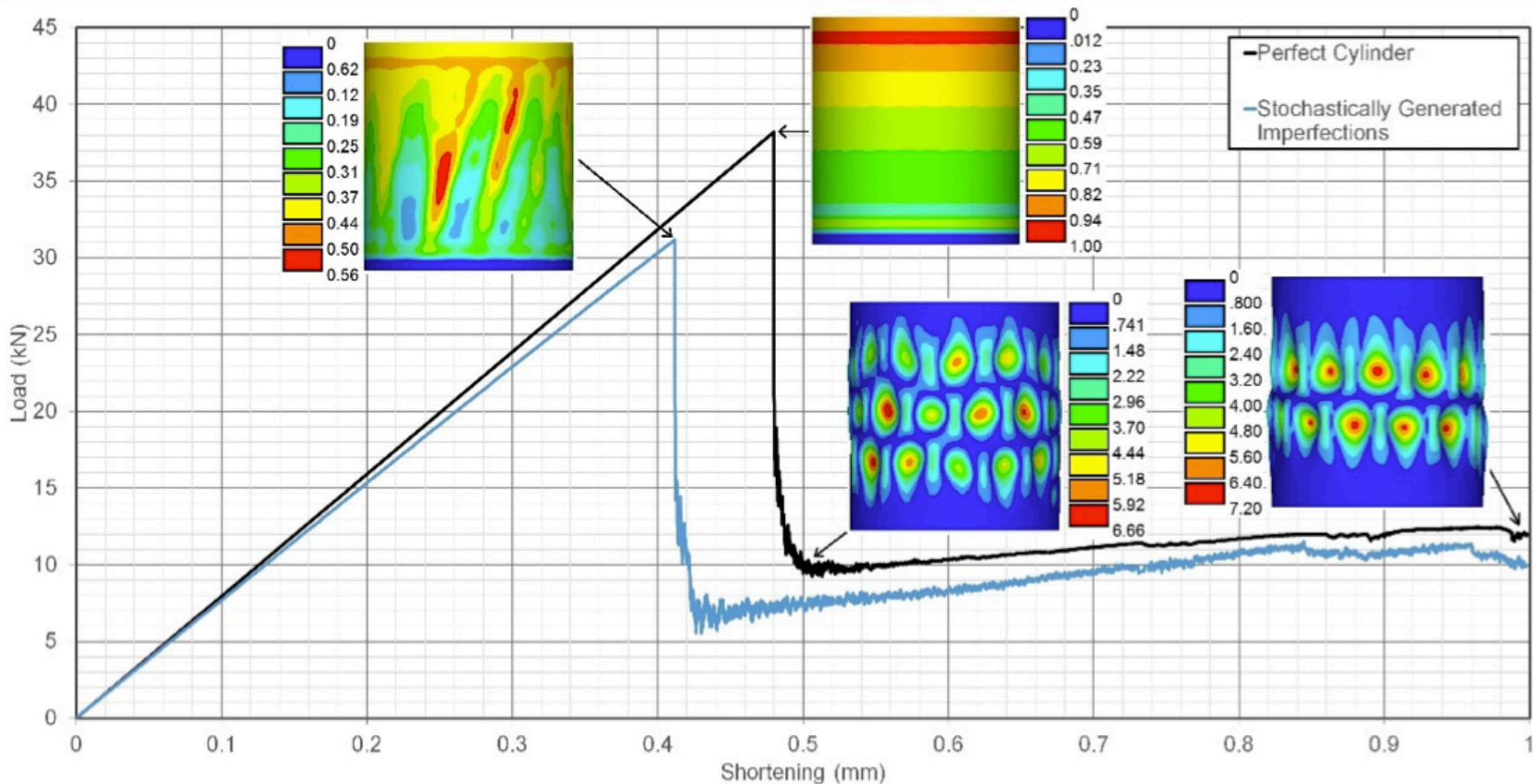


Figure 25. Load-shortening results from finite-element analysis of perfect cylinder and cylinder with stochastically generated thickness imperfections. Scale in mm.



Numerical Results

- Material properties calculated for 100 stochastically generated cylinders using moving window averaging technique.
- Buckling loads for 100 virtual cylinders shown in Figure 25.
- Compared to the perfect numerical buckling load, the buckling loads with geometric and thickness imperfections [19], and the experimental buckling loads [7,19].
- Thickness imperfections influence the buckling load of the cylinders significantly. Can vary between 29.5 and 40kN from a perfect buckling load of 38.2kN.
- When thickness imperfections are combined with geometric imperfections [19], the loads are reduced to a range of 25.0 to 33.3kN.

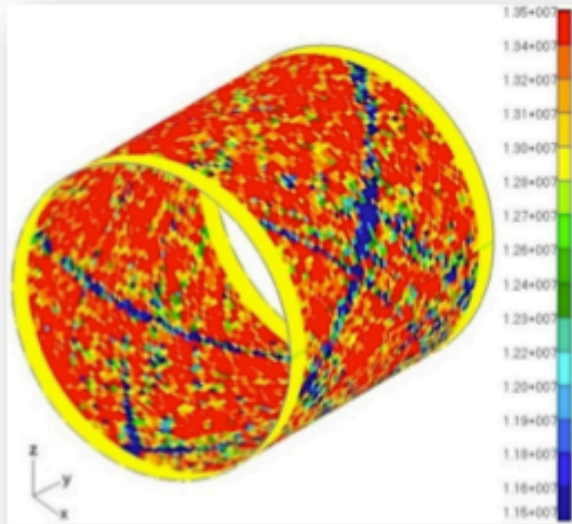


Figure 26. A11 evolution mapped onto elements of FE shell. Scale in N/m.

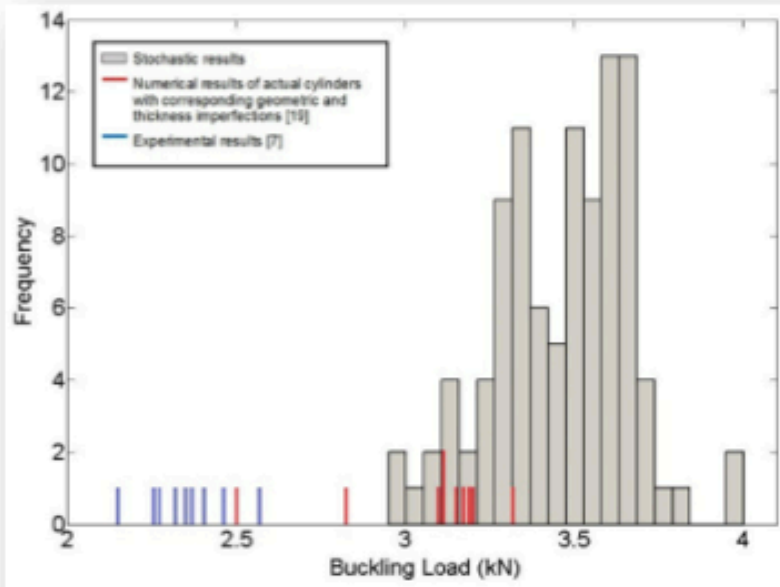


Figure 27. Results of numerical buckling analysis from stochastically generated thickness imperfections.



Numerical Results

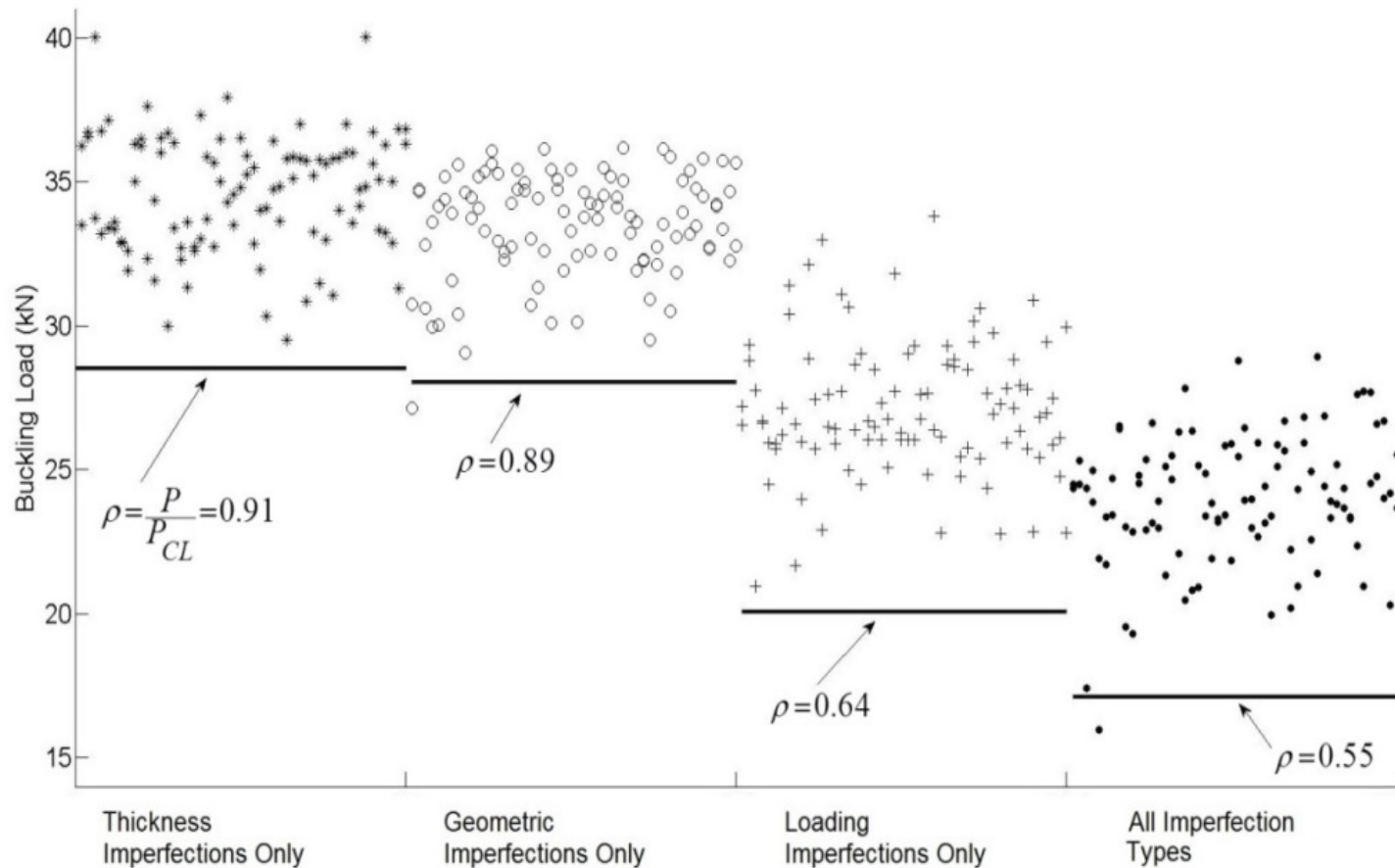


Figure 28. Results of knockdown factors from numerical buckling analysis of stochastically generated imperfections.



Comparing Numerical Results with Experiments

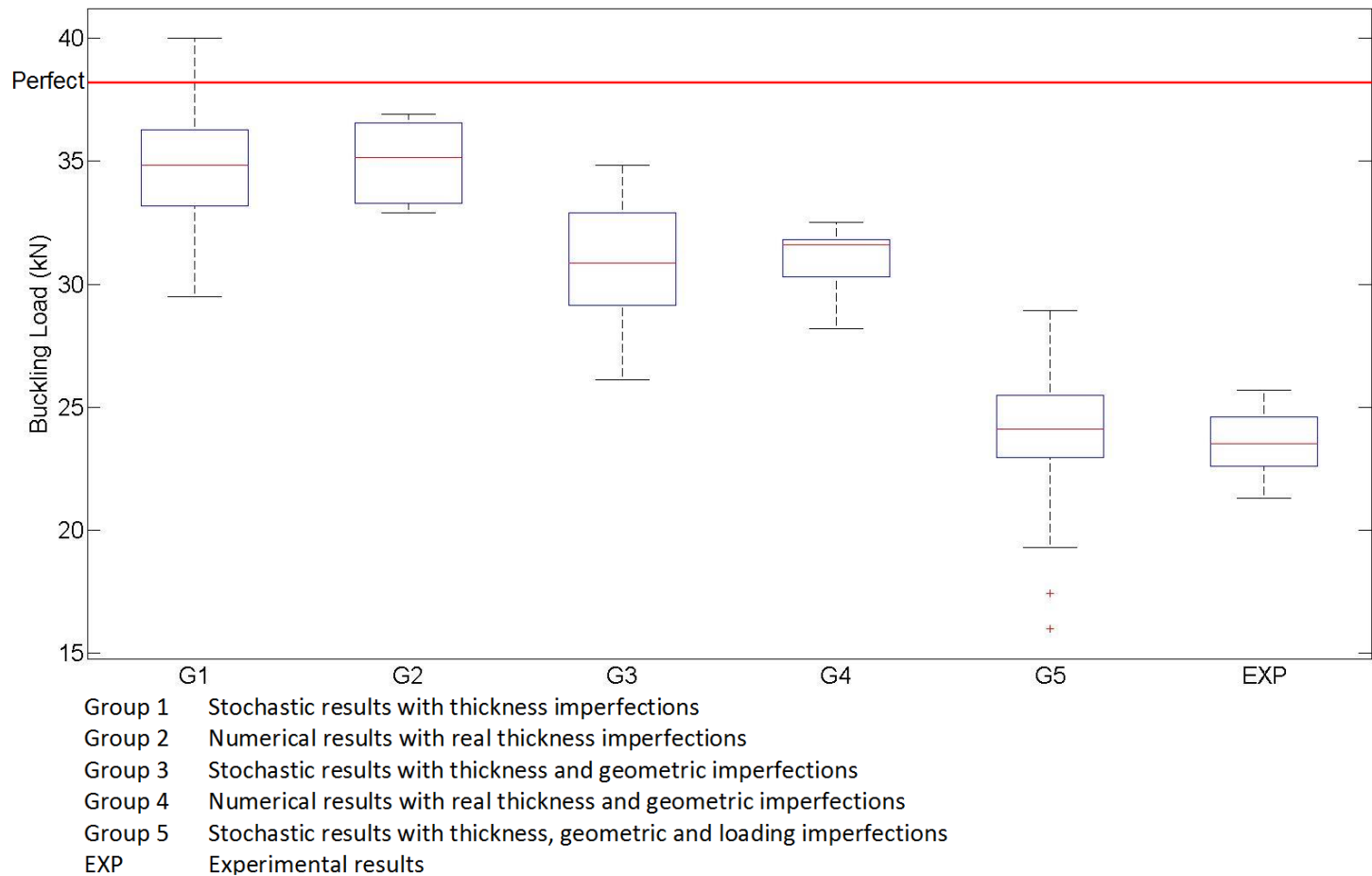


Figure 29. **Box plots of FE simulation and test results.**



Application to Truncated Cones

Cones of various semi-vertex angles and lay-ups selected:

Top Radius, R_{top}	200mm
Bottom Radius, R_{bot}	400mm
Semi-vertex angle, α	5, 15, 30, 45, 60, 75
Orthotropic	$[+30 / -30 / -60 / +60 / 0 / +60 / -60 / -30 / +30]$
Cross-ply	$[0 / 90 / 0 / 90 / 90 / 90 / 0 / 90 / 0]$
Quasi-isotropic	$[0 / 90 / +45 / -45 / 0 / -45 / +45 / 90 / 0]$
CFRP IM7/8552	Longitudinal Young's modulus, $E_{1,c}$ (GPa): 157.4 Transverse Young's modulus $E_{2,c}$ (GPa): 10.1 Shear modulus, $G_{12,c}$ (GPa): 5.3 Shear modulus, $G_{23,c}$ (GPa): 4.0 Ply thickness: 0.125mm

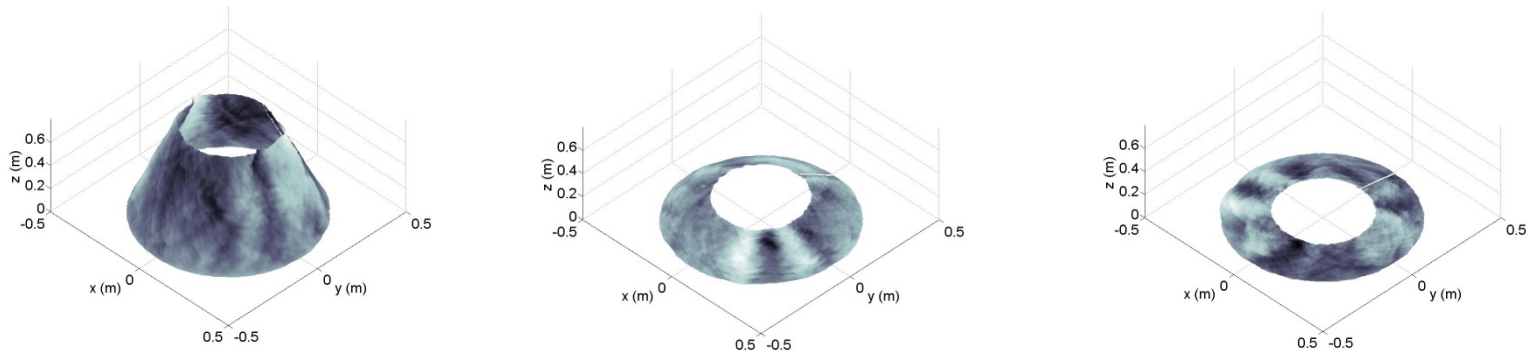


Figure 30. Surface generated imperfections on truncated cones with semi-vertex angles (a) $\alpha = 15^\circ$, (b) $\alpha = 45^\circ$ and (c) $\alpha = 75^\circ$.



Numerical Results

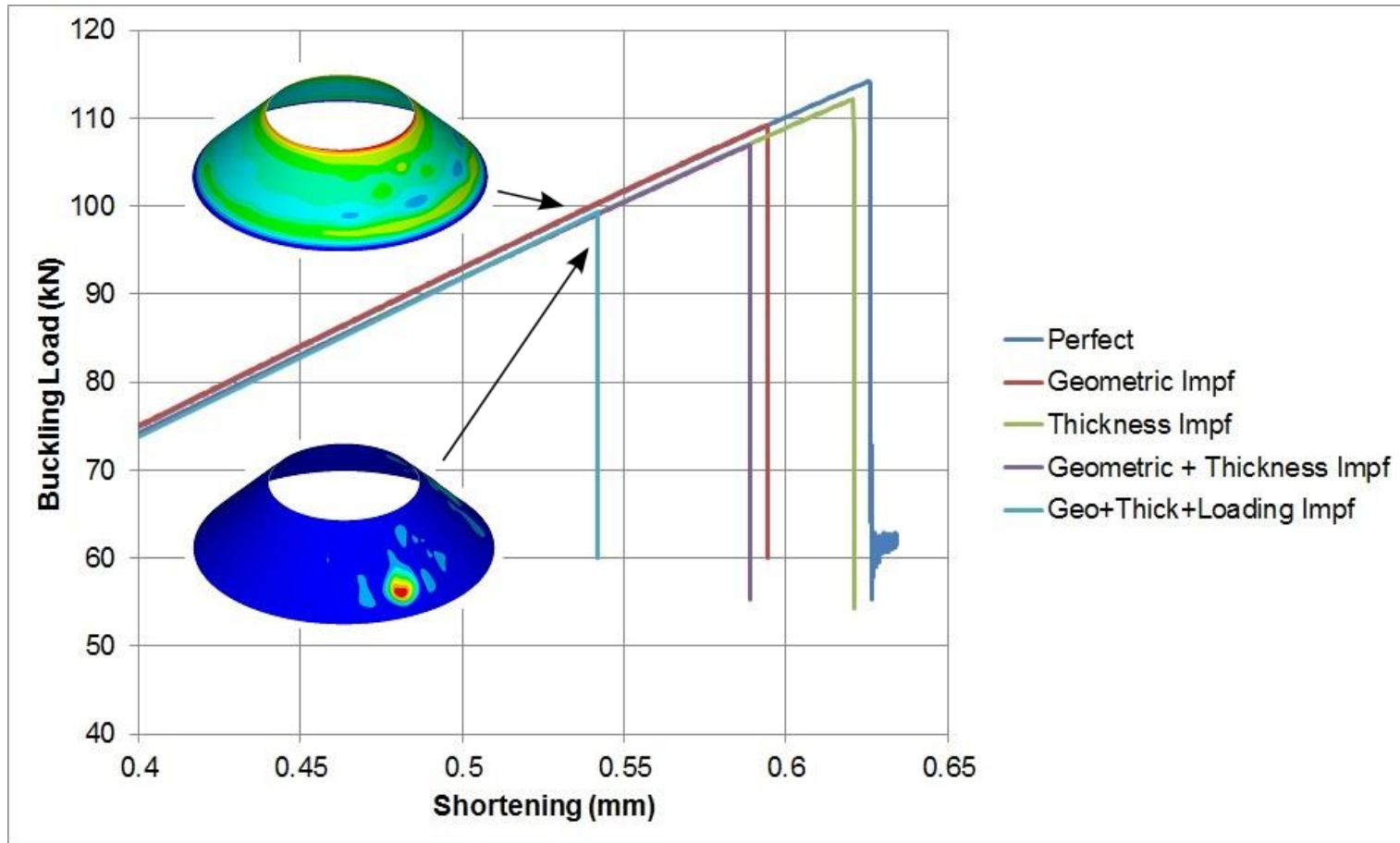
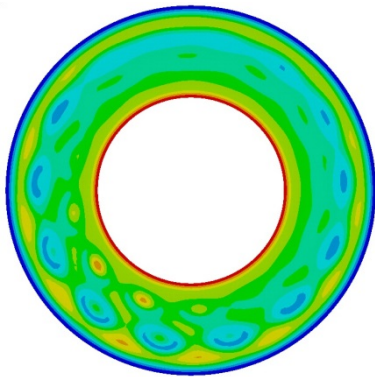


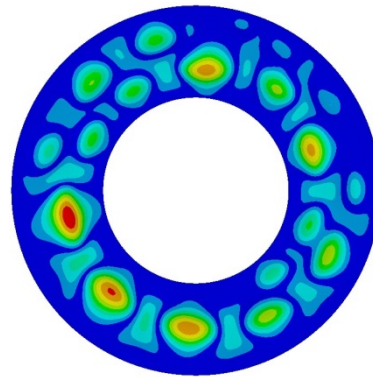
Figure 31. Load-displacement curves of perfect and imperfect truncated orthotropic cones with a semi-vertex angle of $\alpha = 45^\circ$.



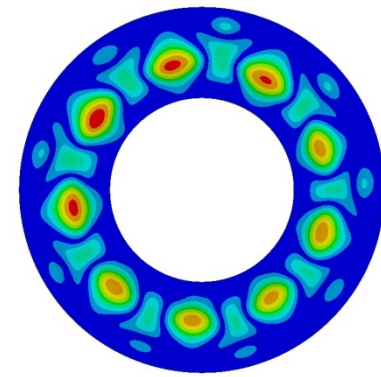
Numerical Results



(a)

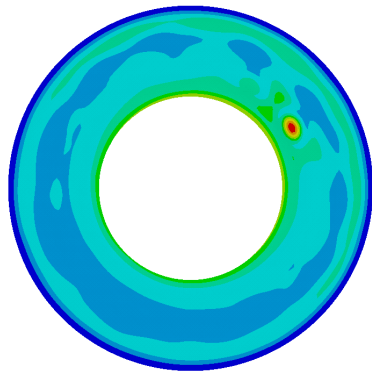


(b)

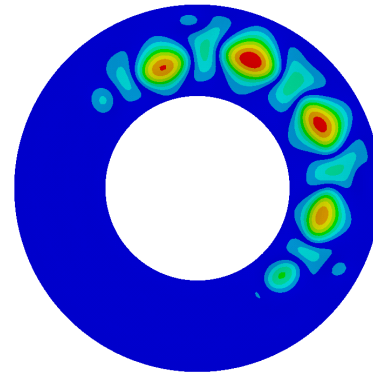


(c)

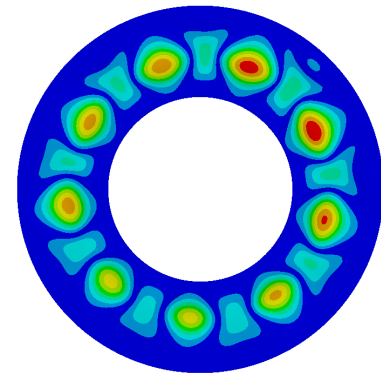
Figure 32. View from the top down: passage of buckling of geometrically perfect orthotropic cone with semi-vertex angle of $\alpha = 45^\circ$, (a) buckling begins, (b) spreads out and (c) encompasses the full cone with 9 circumferential half-waves.



(a)



(b)



(c)

Figure 33. View from the top down: passage of buckling of imperfect orthotropic cone with semi-vertex angle of $\alpha = 45^\circ$, (a) buckling begins at one point, (b) spreads out and (c) encompasses the full cone with 9 circumferential half-waves.



Orthotropic Results

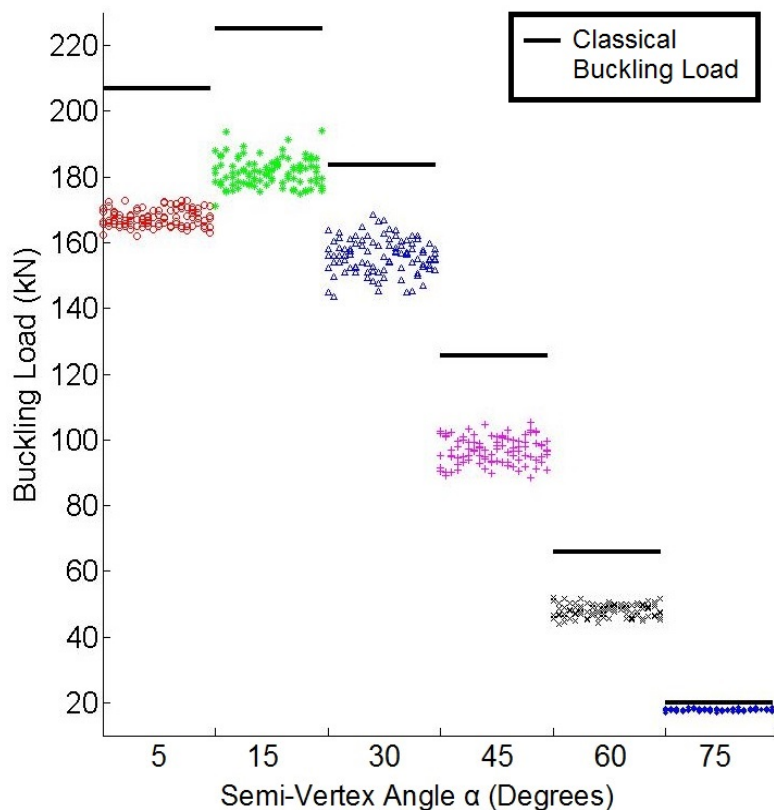


Figure 34. Scatter of buckling loads from stochastic analysis of orthotropic truncated cones at $\alpha = 5, 15, 30, 45, 60$ and 75 compared with the classical buckling load.

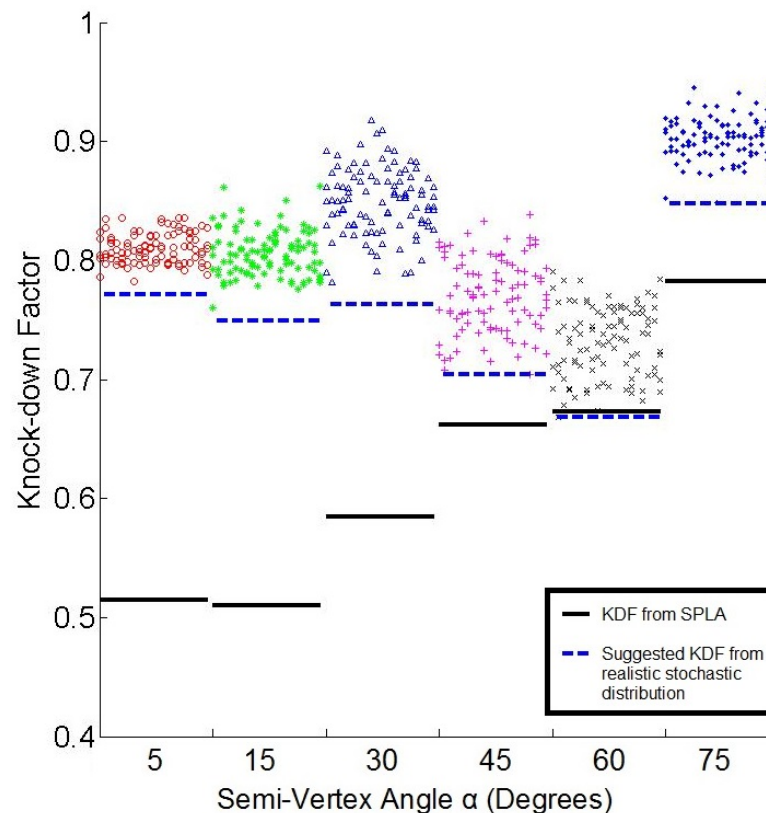


Figure 35. KDFs from applying SPLA on orthotropic truncated cones at $\alpha = 5, 15, 30, 45, 60$ and 75 compared with stochastic results.



Cross-ply Results

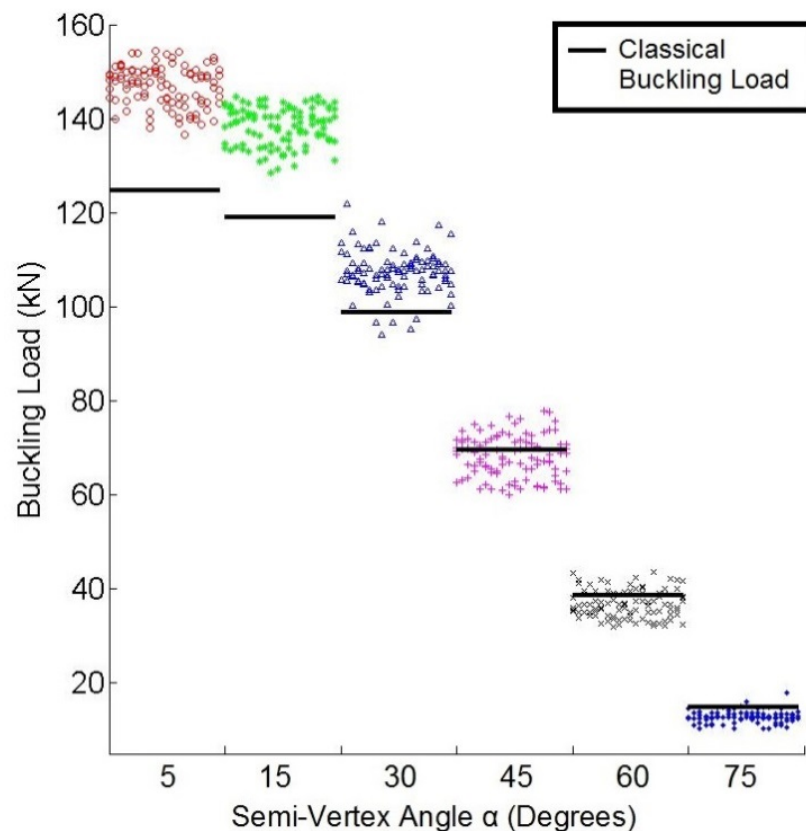


Figure 36. Scatter of buckling loads from stochastic analysis of cross-ply truncated cones at $\alpha = 5^\circ, 15^\circ, 30^\circ, 45^\circ, 60^\circ$ and 75° compared with the classical buckling load.

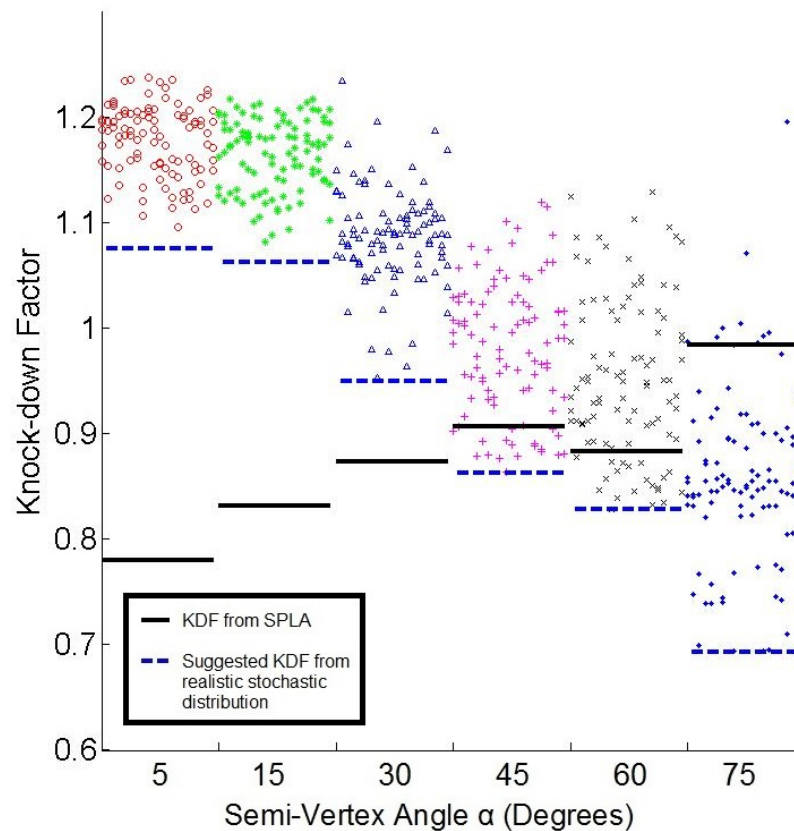


Figure 37. KDFs from applying SPLA on cross-ply truncated cones at $\alpha = 5^\circ, 15^\circ, 30^\circ, 45^\circ, 60^\circ$ and 75° compared with stochastic results.



Quasi-isotropic Lay-up

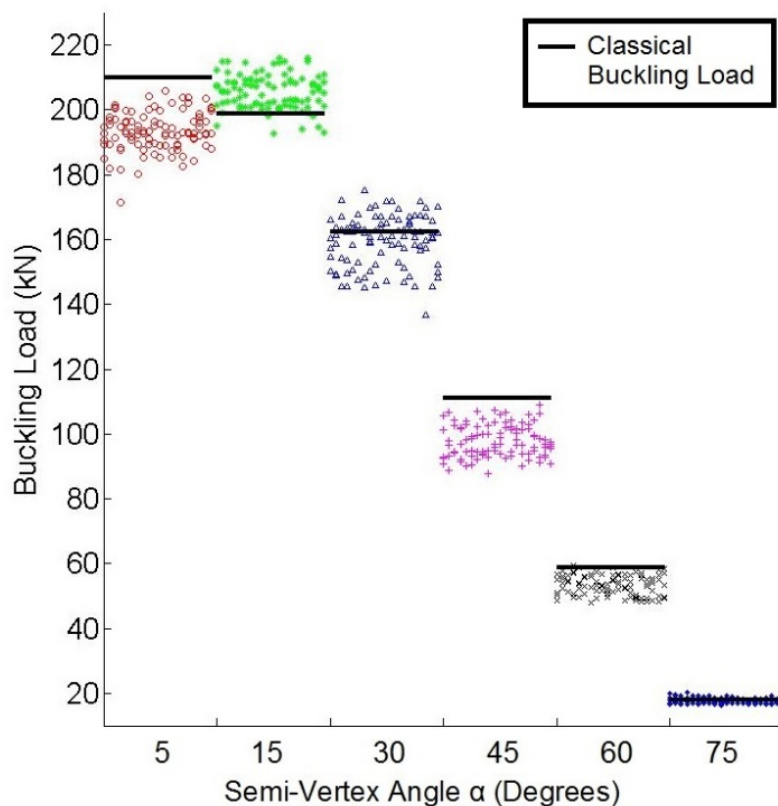


Figure 38. Scatter of buckling loads from stochastic analysis of quasi-isotropic truncated cones at $\alpha = 5^\circ, 15^\circ, 30^\circ, 45^\circ, 60^\circ$ and 75° compared with the classical buckling load.

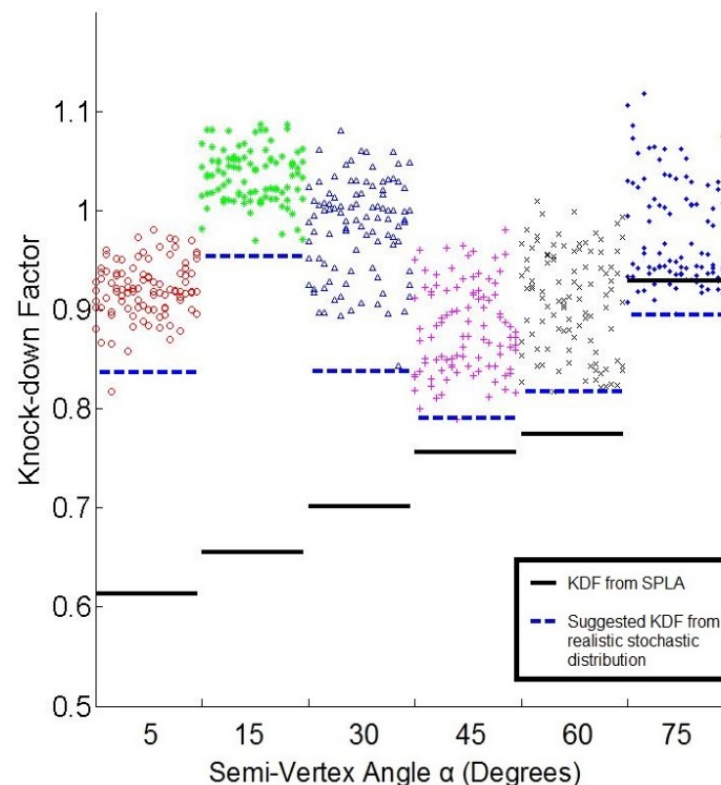


Figure 39. KDFs from applying SPLA on quasi-isotropic truncated cones at $\alpha = 5^\circ, 15^\circ, 30^\circ, 45^\circ, 60^\circ$ and 75° compared with stochastic results.



Conclusion and Future Work

- Material imperfections generated from the stochastic analysis are representative of the actual measured shells.
- The size of the knock-down introduced from thickness imperfections is smaller than that found from geometric and thickness imperfections [19].
- The buckling KDFs determined using stochastic analysis and the SPLA compared well for conical shells of a certain range of lengths or semi-vertex angles, in this case between 0.155m - 0.2m or $\alpha = 45^\circ - 60^\circ$.
- More simulations would be required to confirm this and should vary the top and bottom radii to determine whether the methods are suitable for either a particular range of heights or semi-vertex angles.
- As no experimental data for loading, thickness, material and geometric imperfections were available for the truncated conical structures; the results of the stochastic analyses rely on data from unstiffened CFRP cylinders.
- Employing actual imperfection data from conical structures would further increase the accuracy of the stochastic analysis results.



References



- [1] Ziemian RD. A Guide to Stability Design Criteria for Metal Structures. 6th ed. New Jersey: John Wiley & Sons, Inc.; 2010.
- [2] Kollár L, Dulácska E. Buckling of Shells for Engineers. 1st ed. Budapest: Akademiai Kiado; 1984.
- [3] Koiter WT. The Stability of Elastic Equilibrium. TU-Delft, 1945.
- [4] Von Kármán T, Tsien H. The Buckling of Thin Cylindrical Shells Under Axial Compression. J Aeronaut Sci 1941;8:303–12.
- [5] Donnell LH, Wan CC. Effect of Imperfections on Buckling Analysis of Thin Cylinders and Columns Under Axial Compression. J Appl Mech 1950;17:73–83.
- [6] Bushnell D. Buckling of Shells - Pitfall for Designers. AIAA J 1981;19.
- [7] Degenhardt R, Kling A, Bethge A, Orf J, Kärger L, Zimmermann R, et al. Investigations on imperfection sensitivity and deduction of improved knock-down factors for unstiffened CFRP cylindrical shells. Compos Struct 2010;92:1939–46.
- [8] Degenhardt R. New Robust Design Guideline for Imperfection Sensitive Composite Launcher Structures. Ger Aerosp Cent 2012.
- [9] NASA. Buckling of Thin-Walled Circular Cylinders. 1968.
- [10] Hilburger MW, Nemeth MP, Starnes JH. Shell Buckling Design Criteria Based on Manufacturing Imperfection Signatures. AIAA J 2006;44:654–63.
- [11] Takano A. Improvement of Flügge's Equations for Buckling of Moderately Thick Anisotropic Cylindrical Shells. AIAA J 2008;46:903–11.
- [12] Arbocz J, Hol JMAM. ANILISA - Computational Module for Koiter's Imperfection Sensitivity Theory. Delft, The Netherlands: 1989.
- [13] Tennyson RC. Buckling of Laminated Composite Cylinders: A Review. Composites 1975;6:17–24.
- [14] Chryssanthopoulos MK, Poggi C. Stochastic Imperfection Modelling in Shell Buckling Studies. Thin-Walled Struct 1995;23:179–200.
- [15] Arbocz J, Abramovich H. The Initial Imperfection Data Bank at the Delft University of Technology Part 1. Delft, The Netherlands: 1979.
- [16] Arbocz J, Babcock CD. Experimental investigation of the effect of general imperfection on the buckling of cylindrical shells. 1968.
- [17] Hühne C, Zimmerman R, Rolfes R, Geier B. Sensitivities to Geometrical and Loading Imperfections on Buckling of Composite Cylindrical Shells. Braunschweig: 2002.
- [18] Broggi M. Computational Aspects in the Buckling Analysis of Composite Cylindrical Shells with Random Imperfections Dissertation. Leopold-Franzens-Universität Innsbruck, 2011.
- [19] Broggi M, Schuëller GI. Efficient modeling of imperfections for buckling analysis of composite cylindrical shells. Eng Struct 2011;33:1796–806.
- [20] Lee MCW. Stochastic Analysis and Robust Design of Stiffened Composite Structures. The University of New South Wales, 2009.
- [21] Schillinger D, Papadopoulos V, Papadrakakis M. Evolutionary Power Spectrum Estimation of Strongly Narrow-Band Random Fields. 2nd South-East Eur. Conf. Comput. Mech., Rhodes, Greece: 2009.



References

- [22] Papadopoulos V, Papadrakakis M. The Effect of Material and Thickness Variability on the Buckling Load of Shells with Random Initial Imperfections. *Comput Methods Appl Mech Eng* 2005;194:1405–26.
- [23] Schillinger D, Stefanov D, Stavrev A. The method of separation for evolutionary spectral density estimation of multi-variate and multi-dimensional non-stationary stochastic processes. *Probabilistic Eng Mech* 2013;33:58–78.
- [24] Liang J, Chaudhuri SR, Shinozuka M. Simulation of Nonstationary Stochastic Processes by Spectral Representation. *J Eng Mech* 2007;133:616–27.
- [25] Schillinger D, Papadopoulos V. Accurate estimation of evolutionary power spectra for strongly narrow-band random fields. *Comput Methods Appl Mech Eng* 2010;199:947–60.
- [26] Degenhardt R, Bethge A, Kärger L. Probabilistic aspects of buckling knock down factors—test and analysis. 2007.
- [27] Duda RO, Hart PE. Use of the Hough transformation to detect lines and curves in pictures. *Commun ACM* 1972;15:11–5.
- [28] Cohen L. *Time Frequency Analysis: Theory and Applications*. Englewood Cliffs, NJ: Prentice Hall; 1995.
- [29] Spanos PD, Tezcan J, Tratskas P. Stochastic Processes Evolutionary Spectrum Estimation via Harmonic Wavelets. *Comput Methods Appl Mech Eng* 2005;194:1367–83.
- [30] Stefanou G, Papadrakakis M. Assessment of spectral representation and Karhunen–Loève expansion methods for the simulation of Gaussian stochastic fields. *Comput Methods Appl Mech Eng* 2007;196:2465–77.
- [31] Papoulis A, Pillai S. *Probability, Random Variables and Stochastic Processes*. New York: McGraw-Hill; 2002.
- [32] Graham LL, Gurley K, Masters F. Non-Gaussian simulation of local material properties based on a moving-window technique. *Probabilistic Eng Mech* 2003;18:223–34.



Acknowledgements

This research was supported by the European Commission 7th Framework Program project DESICOS: New Robust Design Guidelines for Imperfection Sensitive Composite Launcher Structures, which is gratefully acknowledged by the authors. This work is part of the research program of the Cooperative Research Centre for Advanced Composite Structures established and supported under the Australian Government Cooperative Research Centres Program.



Thank You

<http://www.crc-accs.com.au>



An Australian Government Initiative

